Adhesive strength improvement by providing steps in joints and differentiating initial and final debonding stresses

Nao-Aki Noda [a,*], Rei Takaki [b,*]

[a] Mechanical Engineering Department, Kyushu Institute of Technology, 1-1 Sensui-cho, Tobata-ku, Kitakyushu-city, Fukuoka 804-8550, Japan
[b] Department of Mechanical and Electrical Engineering, Nippon Bunri University, 1727 Ichigi, Oita-Shi, Oita 870-0397, Japan

ARTICLE INFO

ABSTRACT

Step adhesive joints have a special characteristic quite different from other joints. When initial delamination occurs in other joints such as butt, lap and scarf joints, final failure always occurs. In these cases, the external stress causing initial delamination $\sigma_c^{Initial}$ is equal to the final failure stress as $\sigma_c^{Final} = \sigma_c^{Initial}$. However, in step joints, the final failure stress σ_c^{Final} can be greater than the initial delamination stress $\sigma_c^{Initial} < \sigma_c^{Final}$. To clarify the adhesive improvement mechanism, first, this paper discusses the ISSF (Intensity of Singular Stress Fields) for fully bonded step joint by varying the number of steps N_S. Second, the singular stress field causing 2nd debonding is discussed by analyzing partially delaminated step joint. The results show that 2nd debonding requires larger external load than the initial debonding as $\sigma_c^{Initial} < \sigma_c^{Final}$. This is because under the same external load the singular stress causing the 2nd debonding is smaller than the one causing the initial debonding. When $N_S \geq 6$ and suitable overlap length, the final bond strength σ_c^{Final} can be more than 3.6 ~ 4.4 times larger than the initial delamination stress $\sigma_c^{Initial} \ll \sigma_c^{Final}$ resulting in much larger bond strength.

1. Introduction

With the recent demand for energy conservation and its increasing importance, the current automotive industry is trying to use a variety of lightweight materials in the right places. Such multi-materialization is one of the most promising solutions to achieve this goal [1,2]. In multi-materialization, joining these completely different materials is a major challenge to fully exploit the characteristics of each material [1]. Welding, mechanical joining, and adhesive bonding are some of the joining methods that can be used to realize multi-materialization [3]. Among these, adhesive bonding has many advantages such as smooth surfaces, joining dissimilar materials, weight reduction, sealing, and production economics such as reduced equipment costs and man-hours. It is also believed to maintain the structural integrity of the adherend, thereby ensuring the fatigue resistance of the bonded part better than mechanical bonding, which is a major factor in the adoption of adhesive bonding for multi-materials [4,5]. In recent years, the use of electronics has been promoted in a wide range of fields, such as the automotive industry, the aviation industry, and industrial equipment [6–9]. Indeed, hydraulic drive systems are heavy and significantly contribute to the total weight of a vehicle. By electrifying these systems, it is possible to

reduce the vehicle's weight, which can lead to improved fuel efficiency and enhanced performance. Furthermore, electrification allows for a transition to more energy-efficient power transmission systems, which can also reduce environmental impact [10].

In this way, the requirements for semiconductor packaging technology are becoming more diverse and more important with the trend toward smaller size, higher functionality, and higher performance [11,12]. New materials and structures are being actively introduced into the development of electronic components. Thus, adhesive bonding technology is becoming increasingly important in modern industry. However, as the number of dissimilar material bonding interfaces increases by changing the direction of loading and the shape of the bonded joint, a specific singular stress field is formed [13,14] at the edge of each interface due to a mismatch in deformation, and the risk of delamination failure increases. Therefore, proper evaluation of delamination strength is essential to ensure high reliability in adhesive bonding [15,16]. Hattori et al. [17], Koguchi et al. [18,19] and Ikeda et al. [20] have conducted a series of pioneering studies on the interface strength focusing on the stress singularity in electronic devices. In power device packages, a method of mechanically bonding the lead frames that mount the devices to the encapsulating resin by forming microscopic irregularities at

* Corresponding authors.
E-mail addresses: nao592noda@gmail.com (N.-A. Noda), takakire@nbu.ac.jp (R. Takaki).

the bonding interface has been used to improve the bonding strength between the lead frames and the encapsulating resin [21]. Terao et al. investigated the bond strength between the encapsulating resin and nickel plating by forming minute irregularities during electrolytic nickel plating and showed that the bond strength was improved by a factor of four or more by adding irregularities [22].

The authors have explicitly defined ISSF as the Intensity of Singular Stress Field that appears at the interface end. Then, the bond strength of butt joint [23–25], lap joint [26,27] and scarf joint [28] can be expressed as ISSF=constant even if the bonded geometry is changed. This ISSF is equivalent to the stress intensity factor (SIF) in the crack problem, and ISSF=constant is equivalent to fracture toughness = constant in the cracked material. This study deals with the step joint shown in Fig. 1, considering the unique features of this joint, as shown in Section 2. Examples of the practical importance of step joints can be found in aircraft repair [29,30]. This is because adhesively bonded repair patches are mechanically efficient, and they can be quickly applied depending on the size of the repair and the proficiency of the repair technician [29]. In aerospace, where flat surfaces are often required to meet aerodynamic requirements, stepped repair patches are often applied as shown in Fig. 2 [29,30]. This paper will clarify the bond strength improvement of bonded shapes with such stepped areas [31,32].

2. Special aspects of step joint different from other joints

Step joints have some special features compared to other joints and the difference can be described as follows.

1) The joint area is larger than that of an ordinary straight joint, and thus the joint strength can be expected to be improved. Unevenness of the bonding interface can be simulated by changing the number of steps N_S.

2) In other adhesive joints such as butt, lap and scarf joints, the initial delamination stress $\sigma_c^{Initial}$ is equal to the final failure stress as $\sigma_c^{Final} = \sigma_c^{Initial}$. In step joints, however, the final failure stress σ_c^{Final} can be greater than the initial delamination stress as $\sigma_c^{Initial} < \sigma_c^{Final}$.

3) The improvement in bond strength may be discussed through the analysis and experiment of the step joint by investigating the special characters 1) and 2).

In this way, since the importance of the step joint shown in Fig. 1 is well-known, several studies are available including stress analyses by Erdogan [33] and NASA reports [34,35], and experimental study by Mori et al. [31,32]. However, those previous studies [31–35] have not considered yet the ISSFs at corner points and interface ends. As an example, a singular stress field is generated at the adhesive interface end denoted by Point A. The ISSF at Point A controls initial debonding [31,32,36]. Mori et al. [31,32] investigated the adhesive strength of step joint in Fig. 1(a) experimentally and obtained the results in Fig. 3. As shown in Fig. 3, Mori et al showed that the final debonding stress σ_c^{Final} is different from $\sigma_c^{Initial}$ and larger than the initial debonding stress $\sigma_c^{Initial}$ as can be expressed $\sigma_c^{Initial} < \sigma_c^{Final}$. Especially, when N_S is larger as $N_S \geq 6$, σ_c^{Final} is much larger than $\sigma_c^{Initial}$ as can be expressed $\sigma_c^{Initial} \ll \sigma_c^{Final}$. Those experimental results show that after debonding happened from point A under the initial critical stress $\sigma_c^{Initial}$, the debonding stops and larger external stress become necessary.

Therefore, in this paper, partial delaminated step joint in Fig. 1(b) is newly, considered. Then, another singular stress field appearing at Point B is newly focused. By comparing the singular stress fields as well as the ISSFs at point A and Point B, the experimental results $\sigma_c^{Initial} < \sigma_c^{Final}$ in Fig. 3 will be considered. One may think that when N_S is very large, then the step joint becomes a scarf joint. Previously, the authors analyzed the scarf joint strength when two distinct singular stress appear at the interface end [28]. However, those scarf joints [14] always have $\sigma_c^{Final} = \sigma_c^{Initial}$ different from the step joint having $\sigma_c^{Initial} < \sigma_c^{Final}$. Therefore, this paper does not consider the scarf joints equivalent to the step joints
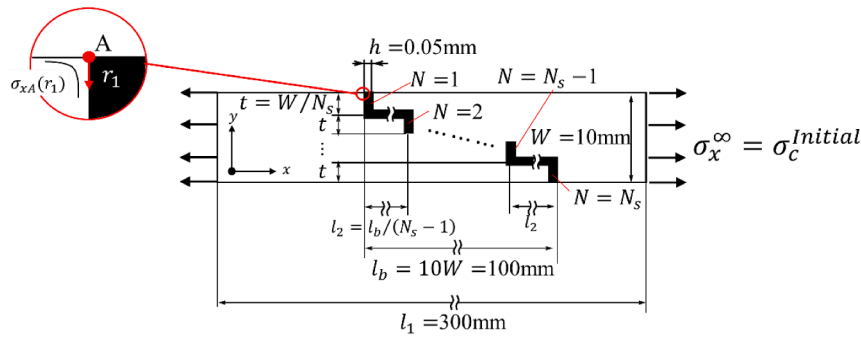
(a) Fully bonded step joint previously studied by Mori et al[31], [32] and newly considered in this study. The ISSF at Point A contributes to initial critical load $\sigma_c^{Initial}$.
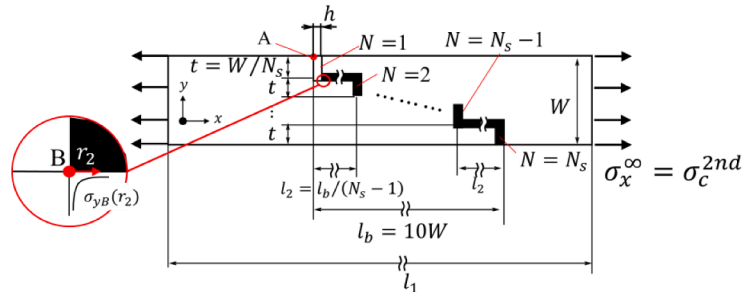
(b) Partially delaminated step joint whose first step is already delaminated. The ISSF at Point B contributes to 2nd debonding load σ_c^{2nd}.

Fig. 1. Step joint consisting of S45C adherend and epoxy resin adhesive. Fig. 1(a), (b) are useful for investigating Fig. 3 where the final debonding load σ_c^{Final} is larger than the initial load $\sigma_c^{Initial} < \sigma_c^{Final}$.
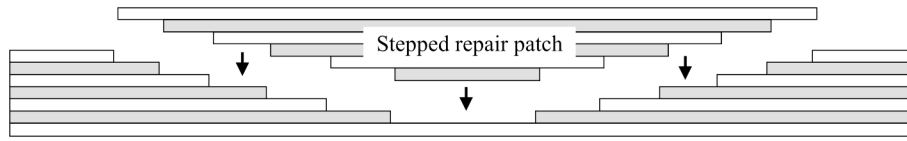
Fig. 2. Step repair patch that meets the aerodynamic requirement of a smooth and flat surface. This step joint consists of a layered CFRP composites adherent and film epoxy adhesive.
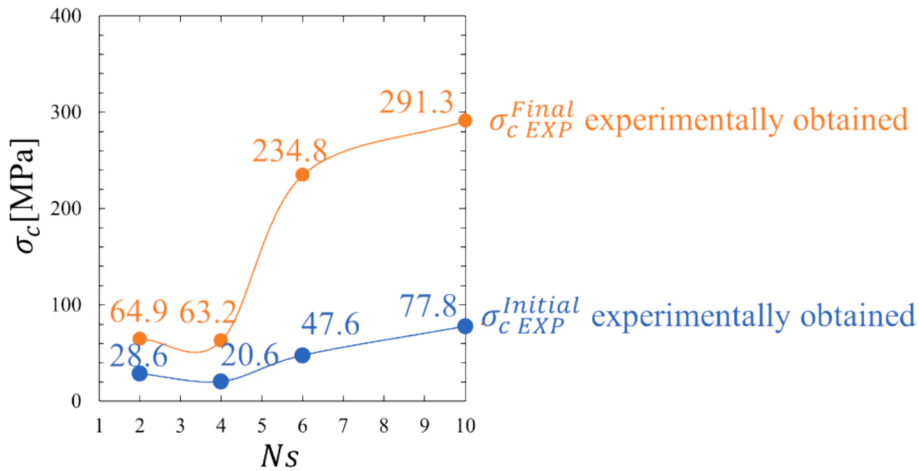

Fig. 3. Final debonding external stress σ_{cEXP}^{Final} that is much larger than initial debonding external stress $\sigma_{cEXP}^{Initial}$ when $N_S \geq 6$ in step joint in Fig. 1(a) obtained experimentally by Mori et al [31,32].

having infinitesimal steps. This paper focuses on the certain finite dimensions of step contributing $\sigma_c^{Initial} < \sigma_c^{Final}$ even when N_S is very large.

3. Singular stress field $\sigma_{xA}(r_1)$ at Point A by analyzing fully bonded step joint

In some adhesive structures, sometimes delamination or interface crack was treated in the category of fracture mechanics. This is because there exists delamination initiation, propagation and the last point of the delaminated area. For each step joint, the stress states corresponding to the initiation, propagation to, e.g., middle point of the step and the last point are different. Recently, except for, e.g., cohesive zone method already incorporated into, e.g., ABAQUS, a new method [37] has occurred in the literature, which is much easier to predict delamination initiation, propagation and the last point of delaminated area. The method [37] described does not require any initial crack in a laminate. It automatically informs whether a laminate/bimaterial under consideration can initiate an interlaminar crack or not. If yes, it can further tell how the initiated delamination will propagate. However, those studies [31–35,37] did not consider the ISSFs at interface ends with no crack explicitly. In other words, conventional fracture mechanics approaches often consider cracks because they cannot treat ISSFs directly. In the fully bonded step joint in Fig. 1(a), different singular stress fields are formed at the interface end A and several corners such as Point B. As shown in Appendix A, the adhesive strength of butt and lap joints can be expressed as a constant ISSF [31,32,36] when there is no crack. Also, as shown in Appendix B, since the singular stress at Point A is larger than the one at Point B, the initial debonding always occurs at the Point A because the singular stress field at Point A is more severe than others. Furthermore, as shown in Appendix C, the mesh-independent ISSF can be analyzed easily by applying the proportional method [23–28]. From Appendix A~Appendix C, the readers may understand that the ISSF method can be applied more usefully and more conveniently than other methods. In this Section, therefore, the singular stress at Point A will be focused when there is no crack.

The geometry of step joints investigated in this study is mainly based on that used in the experiments of Mori et al. [31,32]. Since the dimensionless ISSF defined in this section is determined only by the joint geometry independent of the dimensions, the following discussion is applicable up to the scale for electronic devices. To investigate the effect of the number of steps N_S on the ISSF (Intensity of the singular stress field), the analysis is performed by varying N_S under fixed joint thickness W and overlap length l_b. Specifically, the joint length $l_1 = 300$ mm, thickness $W = 10$ mm, and overlap length $l_b = 100$ mm are fixed, and the number of steps N_S varies as $N_S = 2$, 4, 6, and 10. The thickness of the adhesive layer $h = 0.05$ mm, and the butt length "t" of each step is equal as $t = W/N_S$. The overlap length of the adhesive layer is denoted by l_2, and the overlap length of each tier denoted by l_2 is equal as $l_2 = l_b/(Ns - 1)$. These models were considered in the experiments of Mori et al. [31,32]. In this study, the adhesive layer thickness is fixed as $h = 0.05$ mm and the overlap length is fixed as $l_2 = 10$ mm, $W = 100$ mm. In future studies, the effects of h and l_2 will be investigated considering recent studies [38].

The singular stress field at Point A in Fig. 1(a) is identical to the one at Point A* in Fig. 4. This is because the singular stress field is determined from the local geometry around the Point A (see Fig. 1 and Fig. 4). Therefore, the difference between the stress at Point A and the stress at Point A* can be expressed as the ISSF. Therefore, the ISSFs of the butt joint in Fig. 4 analyzed in previous studies [23,24] can be used as the reference solution in this study (see Appendix A). The stress distribution
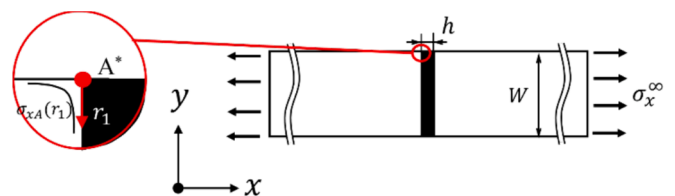

Fig. 4. Reference model for point A.

at the interface around Point A is expressed in Equation (1) from the ISSF at A denoted by K_{σ,λ^A}^A.

$$\sigma_{xA}(r_1) = \frac{K_{\sigma,\lambda^A}^A}{r_1^{1-\lambda^A}} \tag{1}$$

where r_1 is the distance in the y-direction from point A in Fig. 1(a). As shown in equation (1), the interface stress σ_{xA} has a singularity of the form $\sigma_{xA} \propto 1/r_1^{1-\lambda^A}$. The singularity index λ^A at Point A can be obtained as a root of the following characteristic equation (2) [39,40], which can be derived from the local boundary condition around the Point A. Equation (2) always has only one real root, $\lambda^A < 1$, when $\alpha(\alpha - 2\beta) > 0$ [41]. Therefore, the singular stress field at Point A is dominated by the single ISSF K_{σ,λ^A}^A.

$$\left[sin^2\left(\frac{\pi}{2}\lambda^A\right) - \left(\lambda^A\right)^2 \right]^2 \beta^2 + 2\left(\lambda^A\right)^2 \left[sin^2\left(\frac{\pi}{2}\lambda^A\right) - \left(\lambda^A\right)^2 \right] \alpha\beta$$
$$+ \left(\lambda^A\right)^2 \left(\left(\lambda^A\right)^2 - 1\right)\alpha^2 + \frac{sin^2\left(\lambda^A\pi\right)}{4} = 0 \tag{2}$$

where α and β are Dundurs composite parameters and are defined in Equations (3) and (4) from the shear modulus G_j of the adherend and the adhesive and Poisson's ratio ν_j ($j = 1$ for the adherend and $j = 2$ for the adhesive).

Table 1 shows the material properties of adhesive and adherend for step joint in Fig. 1 including E=Young's modulus, ν = Poisson's ratio, σ_B^{Bulk}=Adhesive bulk strength, σ_c^{Butt}=Bulk joint strength in Fig. 4 when h = 0.05 mm, $\tau_{c,l_b=25}^{Lap}$=Lap joint strength in Fig. 10 (c) when l_b = 25 mm, $K_{\sigma c}$ = Critical ISSF, (α, β) = Dundurs parameters, and λ^A, λ_1^B, λ_2^B=Singularity index. The singular stress is characterized by the singularity index, which can be determined from Dundurs parameters as shown in Equation (2). In this study, the ISSFs at interface ends and corner points when there is no crack are focused because the adhesive strength can be expressed as the critical ISSF in Table 1 as shown in Appendix A [31,32,36]

$$\alpha = \frac{G_1(\kappa_2+1) - G_2(\kappa_1+1)}{G_1(\kappa_2+1) + G_2(\kappa_1+1)}, \beta = \frac{G_1(\kappa_2-1) - G_2(\kappa_1-1)}{G_1(\kappa_2+1) + G_2(\kappa_1+1)} \tag{3}$$

$$\kappa_j = \begin{cases} \dfrac{3-\nu_j}{1+\nu_j}(plane\,stress) \\ 3 - 4\nu_j(plane\,strain) \end{cases} (j = 1, 2) \tag{4}$$

The ISSF K_{σ,λ^A}^A at the interface end can be defined in Equation (5). And the dimensionless ISSF F_{σ,λ^A}^A at Point A is defined in Equation (6). Since it is dimensionless, it is the same value for similar geometries and can be applied up to the scale for electronic devices. Here, σ_x^∞ is the far-field tensile stress and h is the thickness of the adhesive layer.

$$K_{\sigma,\lambda^A}^A = \lim_{r \to 0}\left[\sigma_{xA}(r_1) \bullet r^{1-\lambda^A} \right] \tag{5}$$

$$F_\sigma^A = \frac{K_{\sigma,\lambda^A}^A}{\sigma_x^\infty W^{1-\lambda^A}} \tag{6}$$

In the previous studies the proportional method to calculate the ISSF was explained in detail [23–28]. In this study, therefore, how to obtain the exact ISSF is briefly described in Appendix C. Fig. 5 shows the dimensionless ISSF $F_\sigma^A = K_\sigma^A/(\sigma_x^\infty W^{1-\lambda^A})$ at Point A by varying number of steps N_S obtained by fully bonded step joint in Fig. 1(a). In Fig. 5, the ISSF when $N_S = 1$ is equivalent to the result for the butt joint. Compared to the butt joint $N_S = 1$, the value of F_{σ,λ^A}^A is smaller except for the case of the number of steps Ns = 2. Then, F_{σ,λ^A}^A decreases as the number of steps N_S increases. For example, $F_{\sigma,\lambda^A}^A = 0.0760$ for step $N_S = 10$, whereas $F_{\sigma,\lambda^A}^A = 0.0917$ for butt joints. In other words, the value of ISSF at Point A decreases by about 14.5 ~ 16.2 % when $N_S = 10$ compared to the case of butt joint $N_S = 1$.

Fig. 6 illustrates the initial debonding stress $\sigma^{Initial}$ obtained from the ISSF in Fig. 5 in comparison with $\sigma_{cEXP}^{Initial}$ experimentally obtained. In Fig. 5, the light blue line shows $\sigma_c^{Initial}$ and the blue line shows $\sigma_{cEXP}^{Initial}$. From Fig. 3 and Fig. 5, the average critical ISSF can be determined as $K_{\sigma c,ave}^{AInitial} = 7.18 \text{MPa} \bullet \text{mm}^{1-\lambda^A}$ and indicated in Table 1. The initial debonding stress $\sigma_c^{Initial} = K_{\sigma c,ave}^{Initial}/(F_\sigma^A W^{1-\lambda^A})$ in Fig. 6 can be determined from $K_{\sigma c,ave}^{AInitial}$. Similarly, the 2nd delamination stress $\sigma_c^{2nd} = K_{\sigma c,ave}^{2nd}/(F_\sigma^B W^{1-\lambda^B})$ in Fig. 12 in Sections 5 and 6 can be determined from $K_{\sigma c,ave}^{BInitial}$. As shown in Fig. 6, the variation of $\sigma_c^{Initial}$ is approximately the same as the one of $\sigma_{cEXP}^{Initial}$. In previous studies, the authors have shown that the adhesive strength of butt and lap joints can be expressed as a constant ISSF within the standard deviation 10 ~ 20 % [23,24,27]. Instead, Fig. 6 shows that the standard deviation of the step joint is about 50 %, which is much larger than that of other joints. This is probably because the difficulty to determine $\sigma_{cEXP}^{Initial}$ in Fig. 6. The initial delamination occurs at Point A but the strain gauge is attached near Point B due to the difficulty
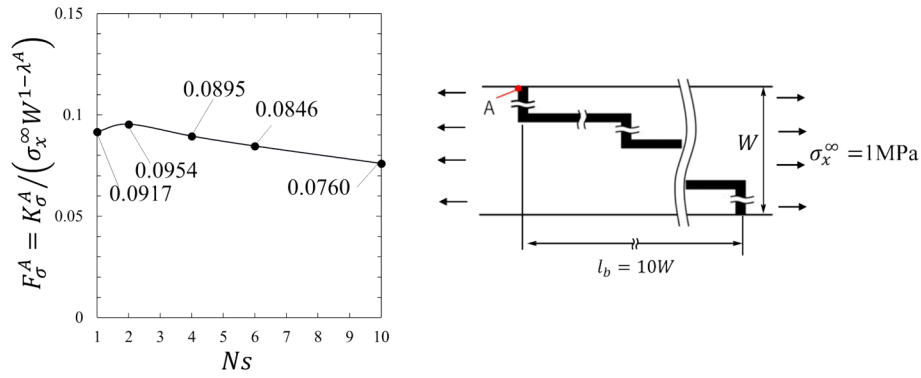
Table 1

Material properties of adhesive and adherend for step joint in Fig. 1 (E=Young's modulus, ν = Poisson's ratio, σ_B^{Bulk}=Adhesive bulk strength, σ_c^{Butt}=Butt joint strength in Fig. 4 when h = 0.05 mm, $\tau_{c,l_b=25}^{Lap}$ = Lap joint strength in Fig. 10(c) when l_b = 25 mm, $K_{\sigma c}$ = Critical ISSF, (α, β) = Dundurs parameters, λ^A, λ_1^B, λ_2^B=Singularity index).

(a) Step joint by Mori et al. [30,31]										
Material	E [GPa]	ν	σ_B^{Bulk} [MPa]	$\sigma_{c,h=0.05}^{Butt}$ [MPa]	$K_{\sigma c}^{Butt}$ [MPa $\bullet$ mm$^{0.296}$]	α	β	λ^A	λ_1^B	λ_2^B
Adherend: S45C	206	0.33	570	39.4	7.18	0.968	0.235	0.704	0.680	0.999
Adhesive: Epoxy resin	3.33	0.34	40							

(b) Reference results in Fig. 10(a), (b) by Naito et al. [6]										
Material	E [GPa]	ν	σ_B^{Bulk} [MPa]	$\sigma_{c,h=0.05}^{Butt}$ [MPa]	$K_{\sigma c}^{Butt}$ [MPa $\bullet$ mm$^{0.260}$]	α	β	λ^A	λ_1^B	λ_2^B
Adherend: Aluminum	68.6	0.33	260	30	6.37	0.894	0.214	0.740	0.664	0.999
Adhesive: Polyimide	3.77	0.342	110							

(c) Reference results in Fig. 10(c) by Park et al. [40]										
Material	E [GPa]	ν	σ_B^{Bulk} [MPa]	$\tau_{c,l_b=25}^{Lap}$ [MPa]	$K_{\sigma c}^{Lap}$ [MPa $\bullet$ mm$^{0.394}$]	α	β	λ^A	λ_1^B	λ_2^B
Adherend: Aluminum	68.9	0.3	260	22.7	61.6	0.870	0.066	0.689	0.606	0.999
Adhesive: Epoxy resin	4.2	0.45	58.7							

Fig. 5. Dimensionless ISSF $F_\sigma^A = K_\sigma^A / (\sigma_x^\infty W^{1-\lambda^A})$ at Point A by varying number of steps N_S obtained by fully bonded step joint in Fig. 1(a).

of attaching near Point A [30,31].

4. Singular stress $\sigma_{yB}(r_2)$ at Point B by analyzing partially delaminated step joint

In the first step delaminated step joint in Fig. 1(b), a singular stress

$$\sigma_{yB}(r_2) = \frac{K_{\sigma,\lambda_1^B}^B}{r_2^{1-\lambda_1^B}} + \frac{K_{\sigma,\lambda_2^B}^B}{r_2^{1-\lambda_2^B}} \tag{7}$$

Here, r_2 is the distance in the x direction from point B (see Fig. 1(b)). The singularity index λ^B at Point B can be obtained from the following characteristic Equation (8) [40,41].

$$4\sin^2(\pi\lambda^B)\left\{\sin^2\left(\frac{\pi\lambda^B}{2}\right) - (\lambda^B)^2\right\}\beta^2 + 4(\lambda^B)^2\sin^2(\pi\lambda^B)\alpha\beta + \left\{\sin^2\left(\frac{\pi\lambda^B}{2}\right) - (\lambda^B)^2\right\}\alpha^2 - 4(\lambda^B)^2\sin^2(\pi\lambda^B)\beta$$
$$-2\left\{(\lambda^B)^2\cos(2\pi\lambda^B) + \sin^2\left(\frac{\pi\lambda^B}{2}\right)\cos(\pi\lambda^B) + \frac{1}{2}\sin^2(\pi\lambda^B)\right\}\alpha + \sin^2\left(\frac{3\pi\lambda^B}{2}\right) - (\lambda^B)^2 = 0 \tag{8}$$

field is formed at Point B. This singular stress field at Point B in Fig. 1(b) is identical to that at Point B* of the lap joint in Fig. 7. The ISSF in Fig. 7 was investigated in previous studies [26,27], which can be used as a reference solution in this study. It is known that two singular stress fields occur in the lap joints [26,27], and the stress distribution around Point $\sigma_{yB}(r_2)$ can be expressed in Equation (7) in terms of two ISSFs $K_{\sigma,\lambda_1^B}^B, K_{\sigma,\lambda_2^B}^B$.
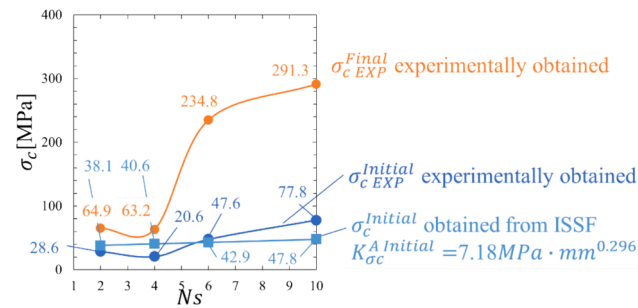

Fig. 6. Initial debonding external stress $\sigma_c^{Initial}$ estimated as $\sigma_c^{Initial} = K_{\sigma c,ave}^{Initial} / (F_\sigma^A W^{1-\lambda^A})$ in comparison with experimentally obtained external stresses $\sigma_{cEXP}^{Initial}$ and σ_{cEXP}^{Final}.

Equation (8) always has two real roots $\lambda_1^B, \lambda_2^B < 1$ [26,27]. However, since $\lambda_2^B \approx 1$, the influence of the second term on the right side of equation (7) can be almost ignored. In other words, the singular stress field at point B can be expressed by one ISSF $K_{\sigma,\lambda_1^B}^B$ as shown in Equation (9) [26,27].

$$\sigma_{yB}(r_2) = \frac{K_{\sigma,\lambda_1^B}^B}{r_2^{1-\lambda_1^B}} + \frac{K_{\sigma,\lambda_2^B}^B}{r_2^{1-\lambda_2^B}} \approx \frac{K_{\sigma,\lambda_1^B}^B}{r_2^{1-\lambda_1^B}} (\because \lambda_2^B \approx 1) \tag{9}$$

The ISSF $K_{\sigma,\lambda_1^B}^B$ at the end of the bonded interface due to adhesive is expressed by Equation (10).

$$K_{\sigma,\lambda_1^B}^B = \lim_{r\to 0}\left[\sigma_{yB}(r_2) \bullet r^{1-\lambda_1^B}\right] \tag{10}$$

Also, the dimensionless ISSF F_σ^B of Point A can be defined in Equation (11). Since F_σ^B is dimensionless, similar shapes always have the same value, and can be applied up to the scale of electronic equipment. Here, σ_x^∞ is the far tensile stress, and h is the adhesive layer thickness.

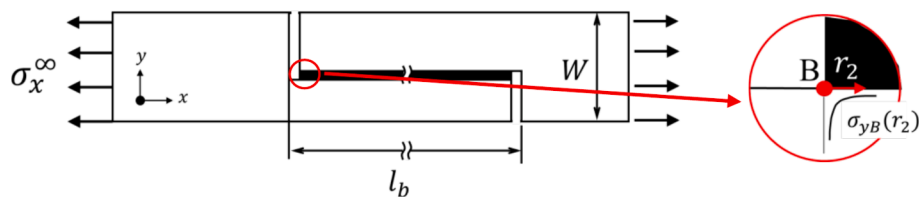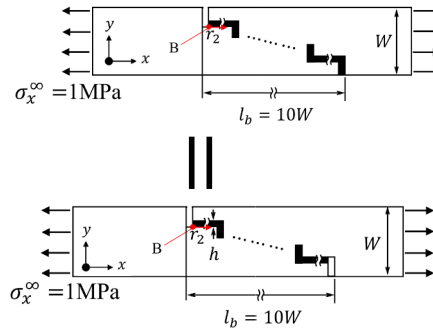$$F_\sigma^B = \frac{K_{\sigma,\lambda_1^B}^B}{\sigma_x^\infty W^{1-\lambda_1^B}} \tag{11}$$

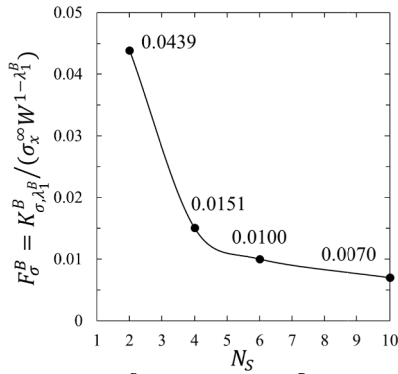**Fig. 7.** Reference model for point B.

(a) The ISSF $F_\sigma^B = K_{\sigma,\lambda_1^B}^B / (\sigma_x^\infty W^{1-\lambda_1^B})$ at Point B in Fig.1(b) The ISSF of partially delaminated model when the last step is also delaminated is shown in the parenthesis.

(b) The ISSF F_σ^B at Point B in Fig. 1(b) coincides with the ISSF of partially delaminated model when the last step is also delaminated as shown in Fig. 8 (b) with an accuracy of 3 digits.

Fig. 8. Dimensionless ISSF $F_\sigma^B = K_{\sigma,\lambda_1^B}^B / (\sigma_x^\infty W^{1-\lambda_1^B})$ at Point B by varying number of steps N_S obtained by partially delaminated step joint in Fig. 1(b).
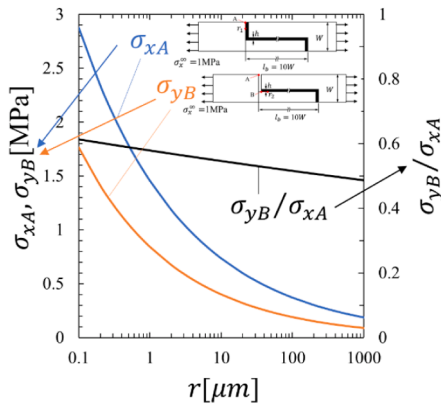
(a) Stress distribution at Point A and Point B when $N_s = 2$
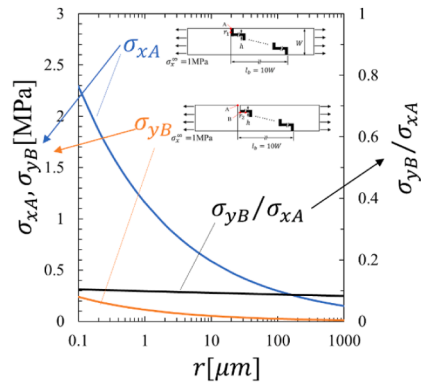
(b) Stress distribution at Point A and Point B when $N_s = 10$
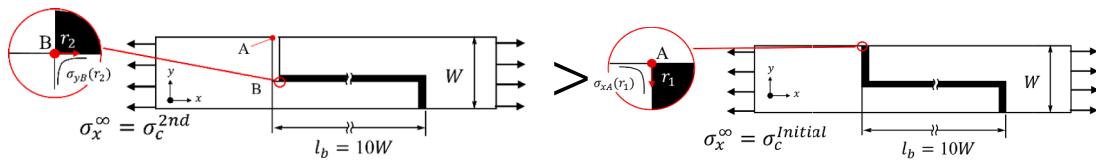
$\sigma_c^{2nd} > \sigma_c^{Initial}$ when $N_s = 2$ from Fig. 8(a)

(c) $\sigma_c^{2nd} > \sigma_c^{Initial}$ when $N_s = 2$
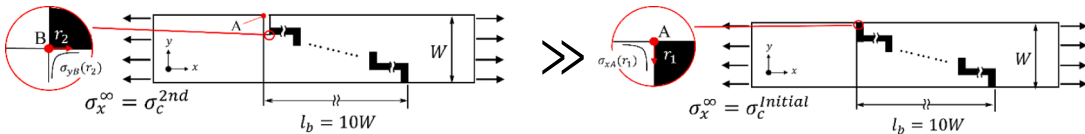
$\sigma_c^{2nd} \gg \sigma_c^{Initial}$ when $N_s = 10$ from Fig. 8(b)

(d) $\sigma_c^{2nd} \gg \sigma_c^{Initial}$ when $N_s = 10$

Fig. 9. Stress distribution σ_{xA} around Point A in fully bonded step joint in comparison with stress distribution σ_{yB} around Point B in partially delaminated step joint.

The outline of the analysis method to calculate the ISSF is described in Appendix B. The method is based on the proportional stress fields for unknown and reference problem. The detail of the method was indicated in previous papers [26,27].

Consider the partially delaminated step joint in Fig. 1(b) where a singular stress field occurs at Point B. The following discussion will be focused on the ISSF at Point B. Fig. 8 shows the ISSF F_σ^B at Point B in the partially delaminated step joint under constant stress loading. As shown in Fig. 8, the ISSF F_σ^B decreases with increasing the number of steps N_s. Unlike the ISSF at Point A obtained from the fully bonded step joint, the ISSF F_σ^B decreases largely with increasing N_s. For example, the ISSF F_σ^B when $N_s = 10$ is only 13.6 % of the ISSF F_σ^B when $N_s = 2$. It should be noted that the ISSF F_σ^B at Point B in Fig. 1(b) coincides with the ISSF of partially delaminated model when the last step is also delaminated as shown in Fig. 8(b) with an accuracy of 3 digits.

Fig. 9 shows the singular stress distribution σ_{yB} at Point B under constant stress $\sigma_x^\infty = 1$MPa obtained by partially delaminated step joint. Then, it is compared with the singular stress σ_{xA} at Point A under constant stress $\sigma_x^\infty = 1$MPa obtained by fully bonded step joint. Since the first step is delaminated, the total adhesive area is smaller than the one of fully bonded case, but as shown in Fig. 9, σ_{yB} is less than σ_{xA}. This is because after the first-step transverse delamination, delamination direction must be changed to the longitudinal direction. As shown in Fig. 9 (b), the difference becomes much larger with increasing the number of steps N_s. For example, when $N_s = 2$, σ_{yB} is about $50 \sim 60$ % of σ_{xA}, whereas when $N_s = 10$, σ_{yB} is only about 10 % of σ_{xA}. Therefore, the adhesive strength σ_c^{2nd} at Point B is larger than the adhesive strength $\sigma_c^{Initial}$ at Point A, and with increasing N_s this trend becomes more significant.

5. Evaluation of second-step delamination stress σ_c^{2nd} at Point B by analyzing partially delaminated step joint

Fig. 10(a) illustrates ABA butt joint and ABA lap joint both consisting of A=Al-alloy, B=Polyimide adhesive. By using the specimens in Fig. 10, Naito et al. [6] compared the tensile bond strength and shear bond
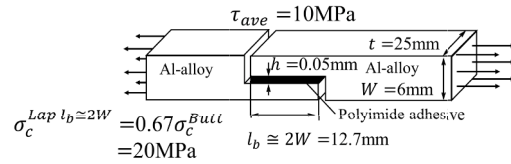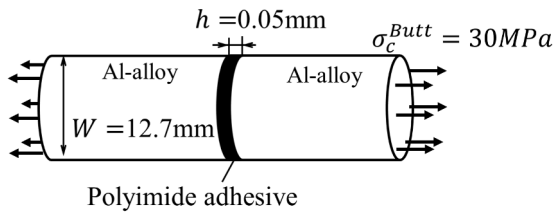
(a) Critical external stresses for butt joint $\sigma_c^{Butt} = P_c/A$, A=51.3mm^2 and for lap joint $\tau_{c,ave}^{Lap\ l_b \cong 2W} = P_c/A$, A=317.5 mm^2 when the adhesive layer thickness h=0.05mm obtained experimentally by Naito et al.[6]. Both ABA butt joint and ABA lap joint are composed of A=Al-alloy, B=Polyimide adhesive.
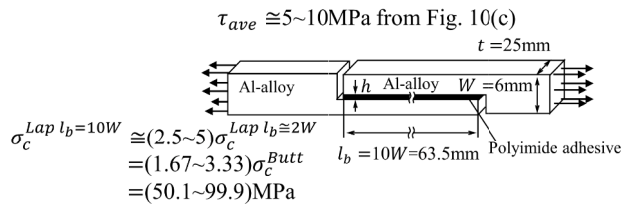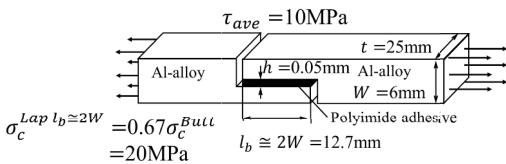
(b) Predicted critical tensile stress $\sigma_c^{Lap\ l_b=10W}$ when the overlap length in Fig. 10(a) is changed to $l_b = 10W$ assuming the same critical average adhesive shear stress $\tau_{c,ave} = P_c/(l_b \times t)$
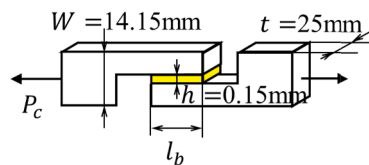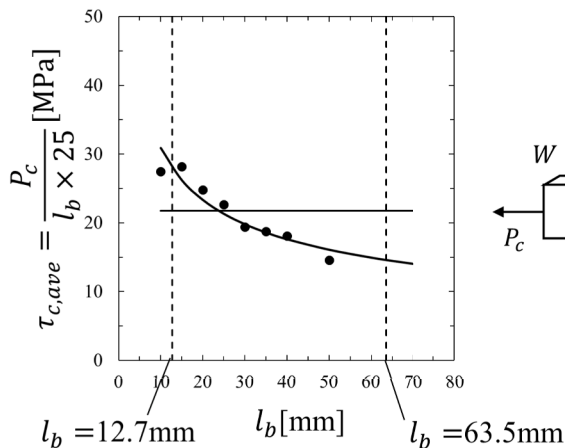
(c) Critical average shear stress $\tau_{c,ave} = \sigma_c/(l_b \times 25)$ by varying adhesive area $A = l_b \times 25$ experimentally obtained by Park et al.[42]

Fig. 10. Critical tensile stress σ_c for butt joint and lap joint with the adhesive area $A = l_b \times t$ obtained by Naito et al.[6].

strength experimentally. As shown in Fig. 10(a), when the adhesive layer thickness $h = 0.05$ mm, the average tensile strength was obtained as $\sigma_c^{Butt} \cong 30$MPa for the cylindrical butt joint in Fig. 10(a). In the lap joint in Fig. 10(a), the cross-section area $A = W \times t$ is half of the adhesive area $A = l_b \times t$ as can be expressed $W \times t = 0.5 \times l_b \times t$. Therefore, the average external strength $\sigma_c^{Lap\ l_b=2W} \cong 20$MPa is 2 times of the average shear strength $\tau_c^{Lap\ l_b=2W} = P_c/(l_b \times t) \cong 10$MPa for the lap joint. Then, $\sigma_c^{Lap\ l_b=2W}$ is approximately 0.67 times of σ_c^{Butt} as can be expressed $\sigma_c^{Lap\ l_b=2W} = 0.67\ \sigma_c^{Butt}$. Fig. 10(a) shows the experimental results of Naito et al. [6] obtained for ABA joints.

Although Naito et al. studied the lap joint when $l_b = 2W$, this study focuses on the step joint in Fig. 1 which Mori et al. investigated when $l_b = 10W$. Therefore, as shown in Fig. 10(b), the lap joint strength when $l_b = 10W$ should be evaluated. Fig. 10(c) shows the average shear strength of the lap joint by varying the overlap length l_b investigated by Park et al. [42]. It is known that the average shear strength $\tau_{c,ave}^{Lap\,l_b=2W}$ is relatively insensitive to the adhesive area [42] or slightly decreases with increasing l_b as shown in Fig. 10(c). In Fig. 10(c), the adhesive shear strength $\tau_{c,ave}^{Lap}$ becomes half with increasing the overlap length l_b from $l_b = 10$ mm to $l_b = 50$ mm. Therefore, by assuming that the bond strength $\tau_{c,ave}^{Lap}$ becomes $0.5 \sim 1$ times with increasing l_b by 5 times as shown in Fig. 10(b), the adhesive strength σ_c can be roughly evaluated by $2.5 \sim 5$ times as $\sigma_c^{Lap\ l_b=10W} = (2.5 \sim\ )\sigma_c^{Lap\ l_b=2W} = (1.67 \sim\ )\sigma_c^{Butt}$. In this way, in the following discussion, $\sigma_c^{Lap\ l_b=10W} = (1.67 \sim 3.33)\sigma_c^{Butt}$ will be assumed. One may think that the average shear strength $\tau_{c,ave}^{Lap}$ decreases as shown in Fig. 10(c) affected by the secondary bending. However, the authors have shown that the bending effect has been included in the ISSF analyzed and bending effects become smaller if the adherend thickness is sufficiently large as shown in the previous paper for lap joints [27].

Fig. 11 summarize the adhesive strength of the butt joint, lap joint, and step joint considered in this study. In Section 3, the initial debonding
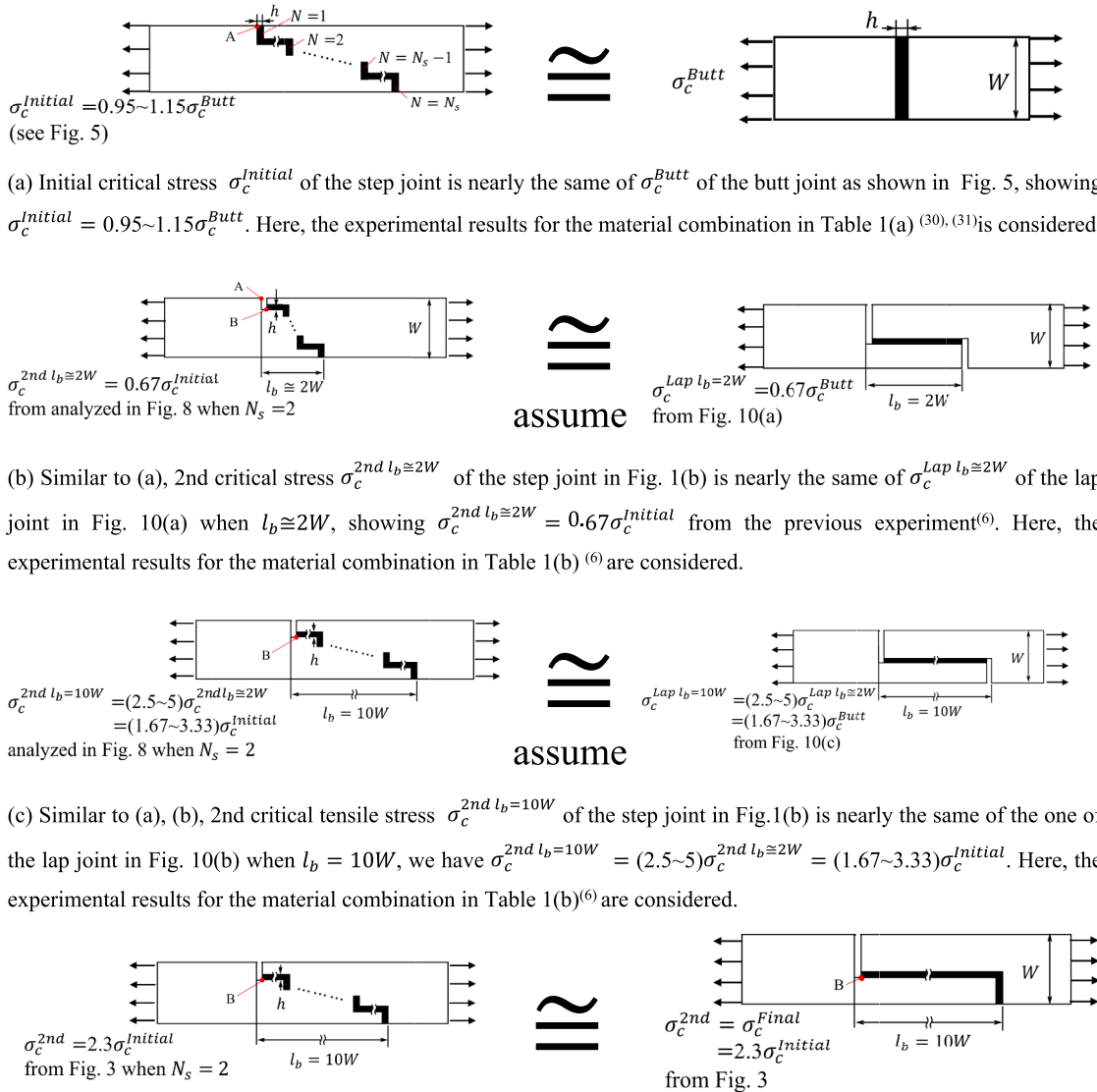

$\sigma_c^{Initial} = 0.95 \sim 1.15 \sigma_c^{Butt}$
(see Fig. 5)

(a) Initial critical stress $\sigma_c^{Initial}$ of the step joint is nearly the same of σ_c^{Butt} of the butt joint as shown in Fig. 5, showing $\sigma_c^{Initial} = 0.95 \sim 1.15 \sigma_c^{Butt}$. Here, the experimental results for the material combination in Table 1(a) [30], [31] is considered.

$\sigma_c^{2nd\ l_b \cong 2W} = 0.67 \sigma_c^{Initial}$
from analyzed in Fig. 8 when $N_s = 2$

assume

$\sigma_c^{Lap\ l_b=2W} = 0.67 \sigma_c^{Butt}$
from Fig. 10(a)

(b) Similar to (a), 2nd critical stress $\sigma_c^{2nd\ l_b \cong 2W}$ of the step joint in Fig. 1(b) is nearly the same of $\sigma_c^{Lap\ l_b \cong 2W}$ of the lap joint in Fig. 10(a) when $l_b \cong 2W$, showing $\sigma_c^{2nd\ l_b \cong 2W} = 0.67 \sigma_c^{Initial}$ from the previous experiment [6]. Here, the experimental results for the material combination in Table 1(b) [6] are considered.

$\sigma_c^{2nd\ l_b=10W} = (2.5 \sim 5)\sigma_c^{2nd\,l_b \cong 2W}$
$= (1.67 \sim 3.33)\sigma_c^{Initial}$
analyzed in Fig. 8 when $N_s = 2$

assume

$\sigma_c^{Lap\ l_b=10W} = (2.5 \sim 5)\sigma_c^{Lap\ l_b \cong 2W}$
$= (1.67 \sim 3.33)\sigma_c^{Butt}$
from Fig. 10(c)

(c) Similar to (a), (b), 2nd critical tensile stress $\sigma_c^{2nd\ l_b=10W}$ of the step joint in Fig.1(b) is nearly the same of the one of the lap joint in Fig. 10(b) when $l_b = 10W$, we have $\sigma_c^{2nd\ l_b=10W} = (2.5 \sim 5)\sigma_c^{2nd\ l_b \cong 2W} = (1.67 \sim 3.33)\sigma_c^{Initial}$. Here, the experimental results for the material combination in Table 1(b) [6] are considered.

$\sigma_c^{2nd} = 2.3 \sigma_c^{Initial}$
from Fig. 3 when $N_s = 2$

assume

$\sigma_c^{2nd} = \sigma_c^{Final}$
$= 2.3 \sigma_c^{Initial}$
from Fig. 3

(d) Second critical tensile stress σ_c^{2nd} of the step joint in Fig.1(b) can be obtained as $\sigma_c^{2nd} = 2.3 \sigma_c^{Initial}$ from Fig. 3 when $N_s = 2$, that is, $\sigma_c^{Initial} = 28.6$MPa, $\sigma_c^{2nd} = \sigma_c^{Final} = 64.9$MPa. Here, the experimental results for the material combination in Table 1(a) [30], [31] is considered.

Fig. 11. Initial critical stress $\sigma_c^{Initial}$ and 2nd critical tensile stress σ_c^{2nd} of the step joint in Fig. 1 (a).

of the fully bonded step joint was discussed. Then, Fig. 5 shows that the analyzed ISSF at Point A of the fully bonded step joint is insensitive to N_s. Based on the results, Fig. 11(a) shows $\sigma_c^{Initial} = (0.95 \sim 1.15)\sigma_c^{Butt}$.

In Sections 4 and 5 above, the 2nd debonding stress σ_c^{2nd} at Point B was considered after the first step is delaminated in Fig. 10 when $l_b \cong 2W$. Then, Fig. 11(b) illustrates $\sigma_c^{2nd\ l_b \cong 2W} = 0.67\sigma_c^{Initial}$ obtained from the following results.

(1) The lap joint strength ISSF can be expressed as the critical ISSF=const. as shown in Fig. A1 in Appendix A.

(2) The 2nd debonding strength $\sigma_c^{2nd\ l_b \cong 2W}$ can be evaluated from the same critical ISSF when $N_S = 2$.

(3) The ISSF of the lap joint and the ISSF of the step joint are equal as shown in Fig. 8.

(4) Based on the same critical ISSF with Fig. 8, $\sigma_c^{2nd\ l_b \cong 2W}$ can be obtained when $N_S \geq 4$ as $\sigma_c^{2nd\ l_b \cong 2W} = 0.67\sigma_c^{Initial}$.

Finally, when $l_b = 10W$, Fig. 11(c) shows that $\sigma_c^{2nd\ l_b=10W} = (2.5 \sim 5)\sigma_c^{2nd\ l_b \cong 2W} = (1.67 \sim 3.33)\sigma_c^{Initial}$ obtained from the following results (5). One may think that using the average stress at failure $\tau_{c,ave} = $ constant $(\sigma_c^{2nd\ l_b=10W} = 5\sigma_c^{2nd\ l_b \cong 2W})$ contradicts using ISSF=constant. However, this study focuses only on 2nd debonding stress σ_c^{2nd}, and 3rd debonding stress σ_c^{3rd} will be the subject in future studies. In this paper, therefore, considering case $\sigma_c^{3rd} > \sigma_c^{2nd}$, the $\tau_{c,ave} = $ constant criterion is taken into account.

(5) Based on the variation of the average shear strength depending on the overlap length l_b in Fig. 10 (c), the 2nd debonding strength when $l_b \cong 10W$ can be evaluated as $\sigma_c^{2nd\ l_b=10W} = (2.5 \sim 5)\sigma_c^{2nd\ l_b \cong 2W}$.

In the above discussion, the experimental data by Naito et al. [6] and Park et al. [42] are mainly considered for evaluating σ_c^{2nd}. More directly, the results of $N_S = 2$ in Fig. 3, that is, $\sigma_c^{Initial} = 28.6$ MPa and $\sigma_c^{Final} = 64.9$ MPa can be used as the data for σ_c^{Final}. Since there are only two steps when $N_S = 2$, 2nd delamination can be the final delamination as $\sigma_c^{2nd} = \sigma_c^{Final}$. Therefore, as shown in Fig. 11(d), $\sigma_c^{2nd} = \sigma_c^{Final} = (64.9/28.6)\sigma_c^{Initial} = 2.3\ \sigma_c^{Initial}$ can be obtained from Fig. 3.

6. Comparison between second-step delamination stress σ_c^{2nd} at Point B and final delamination stress σ_c^{Final}

By applying the results in Section 5, the second step delamination stress σ_c^{2nd} can be evaluated as $\sigma_c^{2nd} = (1.67 \sim 3.33)\ \sigma_c^{Initial}$. Fig. 12 illustrates the second step delamination stress σ_c^{2nd} evaluated from partially delaminated step joint in comparison with the initial and final adhesive strength $\sigma_{cEXP}^{Initial}$ and σ_{cEXP}^{Final} experimentally obtained. Here, the results of σ_c^{2nd} is obtained from ISSF=const. of partially delaminated steeped joint with the results $\sigma_c^{2nd} = (1.67 \sim 3.33)\sigma_c^{Initial}$. For example, when the number of steps N_S increases from $N_S = 2$ to $N_S = 6$, the experimentally obtained final strength σ_{cEXP}^{Final} increases by $(234.8/64.9)$

$= 3.6$ times, while the second step delamination stress σ_c^{2nd} increases by $(169.7/38.8) = 4.4$ times. In this way, the experimental results show that the initial delamination stress $2\sigma_c^{Initial} \approx \sigma_c^{Final}$ when $N_S = 2$ and $3\sigma_c^{Initial} < \sigma_c^{Final}$ when $N_S \geq 6$, the ISSF method can predict this variation consistently. In step joints, the direction of delamination progression must be changed in the lateral and longitudinal directions alternatively. That may result in differentiating the initial, 2nd and 3rd external stresses as can be expressed $\sigma_c^{Initial} < \sigma_c^{2nd} < \sigma_c^{3rd}$. Although, it is not clear whether which critical stress is the largest among $\sigma_c^{2nd}, \sigma_c^{3rd}, \cdots, \sigma_c^{Final}$, the maximum ctrical stress can be difined as σ_c^{Max}. As described in Section 5, if $N_S \geq 6$ and $l_b \geq 10\ W$, the maximum bond strength σ_c^{Max} can be much higher than the other critical stress $\sigma_c^{Initial} \ll \sigma_c^{2nd} \leq \sigma_c^{Max}$ resulting in much larger final bond strength σ_{cEXP}^{Final} from σ_c^{Max}. This knowledge can be used to patch repair of aircraft by applying patches with longer overlap lengths and larger number of steps N_S.

7. Conclusions

Usually if initial debonding occurs in adhesive joints by applying critical external load, the external force causes the final failure as can be expressed $\sigma_c^{Initial} = \sigma_c^{Final}$. In step joints, however, final debonding load can be larger than initial debonding load as $\sigma_c^{Initial} < \sigma_c^{Final}$. To clarify the improvement mechanism in step joints, this study focused on the singular stress fields as well as the ISSFs, which control the adhesive strength. The conclusions can be summarized as follows.

(1) Regarding the fully bonded step joint, the dimensionless ISSF F_σ^A under $\sigma_x^\infty = 1$ MPa decreases slightly with increasing the number of steps N_s. For example, F_σ^A when $N_s = 10$ is 84.8 % of F_σ^A when $N_s = 2$. On the other hand, regarding the partially delaminated step joint focusing on Point B, the ISSF F_σ^B under $\sigma_x^\infty = 1$MPa decreases significantly with increasing N_s. For example, F_σ^B at $N_s = 10$ is only 13.6 % of the ISSF F_σ^B for $N_s = 2$.

(2) The initial debonding stress evaluated from the fully bonded step joint with a constant ISSF agrees well with the initial debonding stress $\sigma_{cEXP}^{Initial}$ (see Fig. 4). Furthermore, the variation of the second debonding stress σ_c^{2nd} evaluated from the partially delaminated step joint agrees well with the variation of the final fracture stress σ_c^{Final} (see Fig. 12).

(3) The reason why the final fracture strength σ_{cEXP}^{Final} is much larger than the initial debonding strength as $\sigma_{cEXP}^{Initial} \ll \sigma_{cEXP}^{Final}$ when $N_S \geq 6$ can be explained as follows. The dimensionless ISSF F_σ^B under a constant load in the partially delaminated step joint decreases largely with increasing N_s (see Fig. 7) although F_σ^A under a constant load in the fully bonded step joint does not change very much (see Fig. 4).

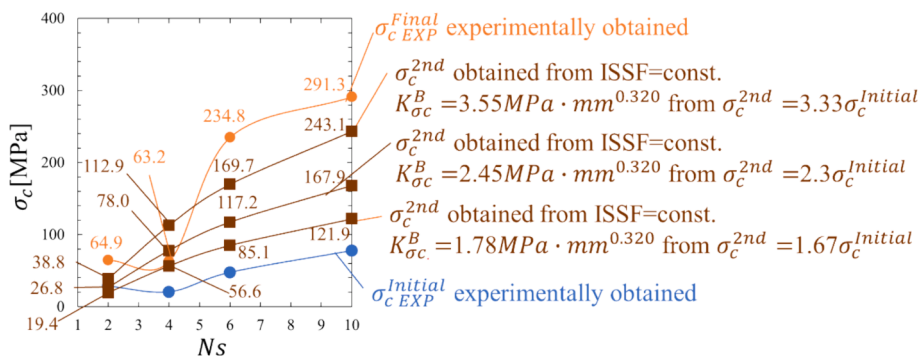**Fig. 12.** Second-step delamination stress evaluated from ISSF $K_{\sigma c}^B = $ constant of partially delaminated steeped joint in comparison with initial critical stress $\sigma_{cEXP}^{Initial}$ and final debonding stress σ_{cEXP}^{Final}.

(4) The reason why the final fracture strength σ_{cEXP}^{Final} is larger than the initial debonding strength as $\sigma_{cEXP}^{Initial} < \sigma_{cEXP}^{Final}$ can be explained as follows. The singular stress distributions σ_{xA} in the fully bonded step joint under a constant load is larger than the singular stress distribution σ_{yB} in the partially delaminated step joint under a constant load as $\sigma_{yB} < \sigma_{xA}$ (see Fig. 9). Since the stress σ_{xA} at Point A is always greater than the stress σ_{yB} at Point B, the 2nd external debonding load σ_c^{2nd} must be larger than the external initial debonding load $\sigma_c^{Initial}$ suggesting that $\sigma_c^{Initial} < \sigma_c^{2nd} < \ldots < \sigma_c^{Max}$. Here, σ_c^{Max} is defined as the maximum debonding stress among $\sigma_c^{2nd}, \sigma_c^{3rd}, \cdots, \sigma_c^{N_S}$.

(5) When $N_S \geq 6$ and $l_b \geq 10\ W$, the final bond strength σ_c^{Final} can be much higher than the initial critical stress $\sigma_c^{Initial} \ll \sigma_c^{Final}$ resulting in much larger bond strength. This knowledge can be used to patch repair of aircraft by applying patches with longer overlap lengths and larger number of steps N_S.

CRediT authorship contribution statement

Nao-Aki Noda: Writing – review & editing, Validation, Supervision, Methodology, Conceptualization. **Rei Takaki:** Writing – review & editing, Writing – original draft, Visualization, Validation, Investigation, Formal analysis, Data curation.

Declaration of competing interest

Data availability

Data will be made available on request.

Appendix A. ISSF of the other adhesive joints

Regarding the butt joint in Fig. A1(a), the critical remote tensile stress $\sigma_y^\infty = \sigma_c$ increases with decreasing the adhesive thickness h. This is because the ISSF under $\sigma_y^\infty = 1$ MPa decreases with decreasing the adhesive thickness h as shown in Fig. A1(b). Note that double singular points exist at the upside/downside interface ends and they interact with each other significantly with decreasing h. In this way, as shown in Fig. A1(c), the adhesive strength can be expressed as a constant ISSF [23]. In the previous studies, the ISSF variation over the entire bondline thickness range was clarified for cylindrical and prismatic butt joints [24]. The validity and usefulness of 2D analysis was confirmed in comparison with 3D analysis [25].

Regarding the lap joint in Fig. A1(d), the critical remote tensile stress $\sigma_x^\infty = \sigma_c$ increases with increasing the overlap length l_b. This is because the ISSF under $\sigma_x^\infty = 1$ MPa decreases with increasing the overlap length l_b as shown in Fig. A1(e). In this way, as shown in Fig. A1(f), the adhesive strength can be expressed as a constant ISSF [27]. Although the lap joints have two singular stress fields that appear at the interface end, the second singularity index $\lambda_2 \cong 1$ and the second singular field is usually negligible [27].
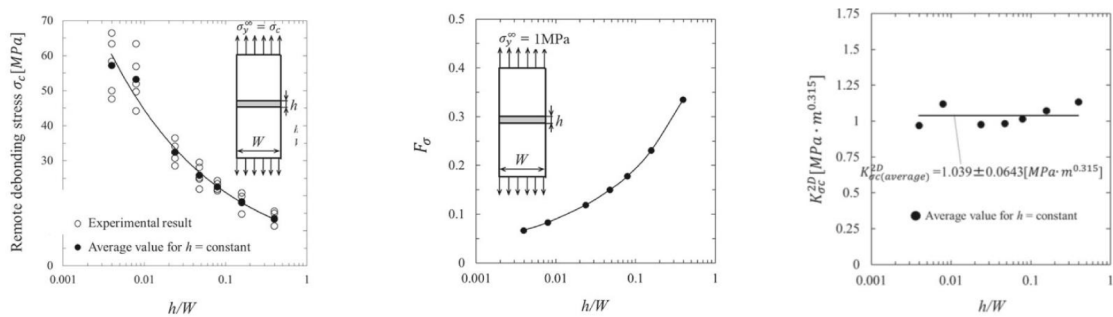
(a) Critical remote tensile stress σ_c for butt joint

(b) ISSF under $\sigma_y^\infty = 1$ MPa for butt joint

(c) Critical ISSF=const. for butt joint
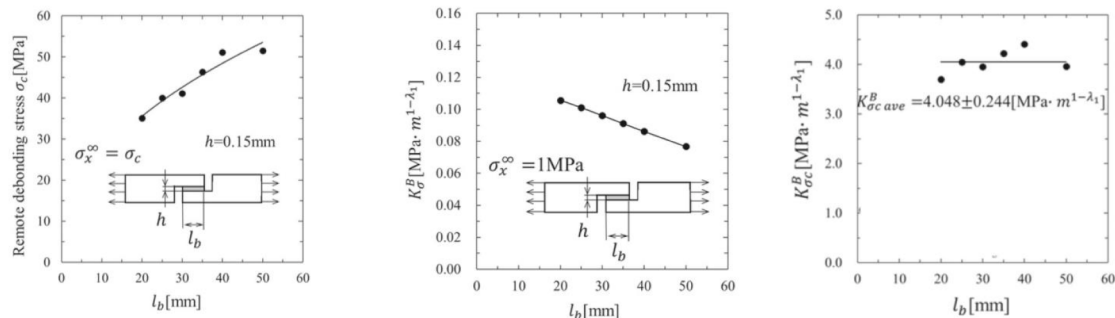
(d) Critical remote tensile stress σ_c for lap joint

(e) ISSF under $\sigma_y^\infty = 1$ MPa for lap joint

(f) Critical ISSF=const. for lap joint

Fig. A1. Prismatic butt joint Resin/S35C whose adhesive strength can be expressed as a constant ISSF [23] and lap joint whose adhesive strength can be expressed as a constant ISSF [27].

Appendix B. Singular stress field at Point B of fully bonded step joint

In this paper, the singular stress field at Point A in Fig. 1 and the one at Point B in Fig. 2 were compared. Then, the results showed that larger external stress is necessary for the 2nd debonding at Point B in Fig. 2. Similarly, even in the fully bonded step joint in Fig. B1, the singular stress also appears at Point B. In this Appendix A, therefore, the singular stress fields at Point B of the fully bonded step joint will be compared with the one at Point A to confirm the initial debonding always occurs at Point A.

Note that the singular stress field at Point B in Fig. A1 is identical to the singular stress field at Point B* of a reinforced fiber in a matrix shown in Fig. B2. The ISSF of Point B* in Fig. B2 was previously analyzed by applying the body force method (BFM). The BFM is a powerful analytical method to obtain accurate solutions, which can be virtually regarded as exact solutions [43,44]. First, a single rectangular inclusion was solved by Chen-Nisitani [45,46]. Next two [47,48] and periodic array of rectangular inclusion [49] were analyzed. The ISSF of a single cylindrical inclusion [50] and periodic array of inclusions [51] were also analyzed. Those results were used to analyze a fiber pull-out test [52,53]. Those studies confirmed that the ISSF at B* in Fig.B2 has been obtained very accurately.

The stress distribution around the corner B can be expressed as shown in Equation (B1) in terms of the ISSFs at Point B, K^B_{σ,λ^B}. As shown in Eq. (B1), there are two singular stress fields, and the singularity index λ has two real roots for most material combinations.
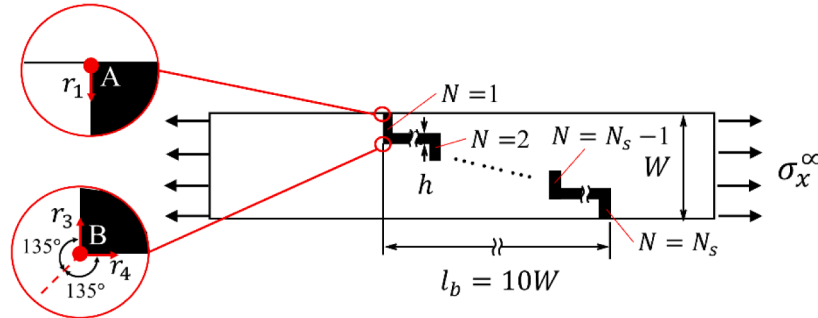

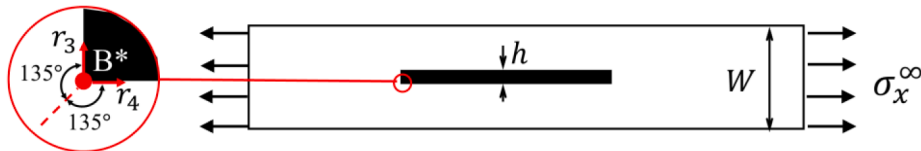Fig. B1. Fully bonded step joint to analyze the ISSF at Point B.

Fig. B2. Reference problem of a rectangular inclusion at Point B* for .

$$\sigma^B_x(r_3) = \frac{K^B_{\sigma,\lambda^B_1}}{r_3^{1-\lambda^B_1}} + \frac{K^B_{\sigma,\lambda^B_2}}{r_3^{1-\lambda^B_2}}$$

$$\sigma^B_y(r_4) = \frac{K^B_{\sigma,\lambda^B_1}}{r_4^{1-\lambda^B_1}} - \frac{K^B_{\sigma,\lambda^B_2}}{r_4^{1-\lambda^B_2}} \tag{B1}$$

Here, r_3 is the distance in the y direction from point B, and r_4 is the distance in the x direction from point B (see Fig. B1).

The singularity index λ^B_1, λ^B_2 at in Eq. (B1) can be obtained from the following characteristic Equations (B2), (B3) [43,44] with the bisector angle $\theta = \pi/2$.

$$(\alpha+\beta)^2 \left(\lambda^B_1\right)^2 [1-\cos(2\theta)] + 2\lambda^B_1(\alpha-\beta)\sin\theta\{\sin(\lambda^B_1\theta) + \sin[\lambda^B_1(2\pi-\theta)]\}$$

$$+ 2\lambda^B_1(\alpha-\beta)\sin\theta\{\sin(\sin[\lambda^B_1(2\pi-\theta)] - \lambda^B_1\theta)\} + (1-\alpha^2) - (1-\beta^2)\cos(2\lambda^B_1\pi)$$

$$+ (\alpha^2-\beta^2)\cos[2\lambda^B_1(\theta-\pi)] = 0 \tag{B2}$$

$$(\alpha+\beta)^2 \left(\lambda^B_2\right)^2 [1-\cos(2\theta)] + 2\lambda^B_2(\alpha-\beta)\sin\theta\{\sin(\lambda^B_2\theta) + \sin[\lambda^B_2(2\pi-\theta)]\}$$

$$+ 2\lambda^B_2(\alpha-\beta)\sin\theta\{\sin(\sin[\lambda^B_2(2\pi-\theta)] - \lambda^B_2\theta)\} + (1-\alpha^2) - (1-\beta^2)\cos(2\lambda^B_2\pi)$$

$$+ (\alpha^2-\beta^2)\cos[2\lambda^B_2(\theta-\pi)] = 0 \tag{B3}$$

The local geometry around Point B is symmetric with respect to the bisector x of B as shown in Fig. B1 [42,43]. Therefore, the singular stress around B can be separated into two types; one is symmetric mode I singular stress field, and the other is skew-symmetric mode II type singular stress field [45–49,52,53] as shown in Equation (B4).

$$2\sigma^B_I(r) = \sigma^B_x(r_3) + \sigma^B_y(r_4),$$

$$2\sigma^B_{II}(r) = \sigma^B_x(r_3) - \sigma^B_y(r_4) \tag{B4}$$

It is known that $\sigma_I^B(r)$ is proportional to $1/r^{1-\lambda_1^B}$ and $\sigma_{II}^B(r)$ is proportional to $1/r^{1-\lambda_2^B}$ as shown in Eq. (B1). Those singular stress distributions are dominated by two distinct ISSFs denoted by $K_{I,\lambda_1^B}^{B*}$ and $K_{II,\lambda_2^B}^{B*}$ as shown in Eq.(1). Two ISSFs can be defined as shown in Eq. (B5). In this equation, we can put $r = r_3 = r_4$.

$$K_{I,\lambda_1^B}^B = \lim_{r \to 0}\left[\sigma_I^B(r) \bullet r^{1-\lambda_1^B}\right],$$

$$K_{II,\lambda_2^B}^B = \lim_{r \to 0}\left[\sigma_{II}^B(r) \bullet r^{1-\lambda_2^B}\right] \tag{B5}$$

In the previous studies, the ISSFs in Fig. B2 were analyzed by the body force method[41]. The dimensionless ISSFs $F_{I,\lambda_1^B}^B$, $F_{II,\lambda_2^B}^B$ at Point B in the step joint in Fig. B1 are expressed as shown in Equation (B6). Since $F_{I,\lambda_1^B}^B$ and $F_{II,\lambda_2^B}^B$ are dimensionless, similar shapes must have the same values, and they can be applied up to the scale of electronic equipment.

$$F_{I,\lambda_1^B}^B = K_{I,\lambda_1^B}^B/(\sigma_x^\infty h^{1-\lambda_1^B}),$$

$$F_{II,\lambda_2^B}^B = K_{II,\lambda_2^B}^B/(\sigma_x^\infty h^{1-\lambda_2^B}) \tag{B6}$$

Regarding the rectangular inclusions in Fig.B2, the dimensionless ISSFs $F_{I,\lambda_1^B}^{B*}$ and $F_{II,\lambda_2^B}^{B*}$ at Point B* in Fig.B2 can be defined in the same way as shown in Eq. (B7) [41]. The exact solution $F_{I,\lambda_1^B}^{B*}$ and $F_{II,\lambda_2^B}^{B*}$ was provided in the previous papers and they can be used as a reference solution to analyze $F_{I,\lambda_1^B}^B$, $F_{II,\lambda_2^B}^B$ in Fig. B1 by applying the same FEM mesh. The detail of this analysis method is indicated in Appendix B.

$$F_{I,\lambda_1^B}^{B*} = K_{I,\lambda_1^B}^{B*}/(\sigma_x^\infty h^{1-\lambda_1^B}),$$

$$F_{II,\lambda_2^B}^{B*} = K_{II,\lambda_2^B}^{B*}/(\sigma_x^\infty h^{1-\lambda_2^B}) \tag{B7}$$

By using the reference solution in Fig. B2, the ISSF of Point B in Fig. B1 can be obtained and can be expressed in Appendix B. Fig. B3 compares the stress $\sigma_x^A(r_3)$ around Point A and the stress $\sigma_x^B(r_3)$ around point B when $N_s = 10$. Here, the stress $\sigma_x^A(r_3)$ was determined from Equation (1) in Section 3 with FEM analysis. And the stress $\sigma_x^B(r_3)$ was determined from Equation (B1) with FEM analysis. As shown in Equation (B8), shows the range Its scope of application is as follows. In other words, the stress $\sigma_x^A(r_1)$ near point A is expressed by equation (B8). On the other hand, the stress $\sigma_x^B(r_3)$ around Point B is expressed in Equation (B9).

$$\sigma_x^A(r_1) = \frac{K_{\sigma,\lambda^A}^A}{r_1^{1-\lambda^A}} \ (\text{r} \le 5.5\mu m),$$

$$\sigma_x^A(r_1) = \sigma_{FEM}^A(r)(\text{r} > 5.5\mu m) \tag{B8}$$

$$\sigma_x^B(r_3) = \frac{K_{I,\lambda_1^B}^B}{r_3^{1-\lambda_1^B}} + \frac{K_{\sigma,\lambda_2^B}^B}{r_3^{1-\lambda_2^B}} \ (\text{r} \le 0.35\mu m),$$

$$\sigma_x^B(r_3) = \sigma_{FEM}^B(r) \ (\text{r} > 0.35\mu m) \tag{B9}$$

3134645895776Comparison between $\sigma_x^A(r_1)$ and $\sigma_x^B(r_3)$ shows that $\sigma_x^A(r_1) > \sigma_x^B(r_3)$ when for $N_s = 2$ 10, and $\sigma_x^A(r_1)$ is about $4 \sim 5$ times larger than $\sigma_x^B(r_3)$. Therefore, it is thought that the initial debonding occurs at Point A. Therefore, the initial debonding occurring at point A can be confirmed.
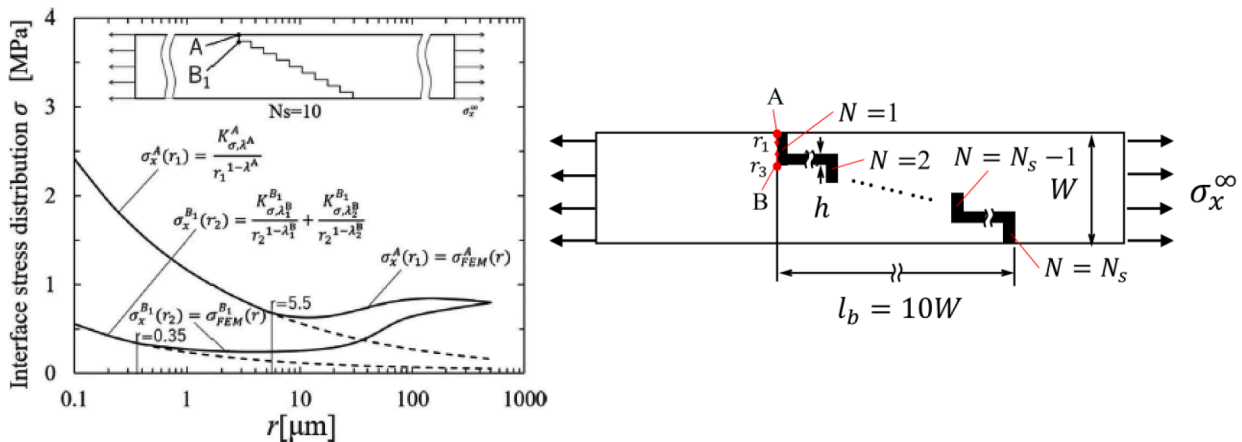

Fig. B3. Comparison between and in fully bonded step joint when.

Appendix C. Mesh independent ISSF analysis method based on the proportional stress field

To obtain the ISSF at the interface end, singular stress must be analyzed very accurately. However, usually FEM stress varies depending on FEM mesh size and it cannot provide the ISSF directly. In the previous study, therefore, by applying the same FEM mesh size and the same FEM mesh pattern, FEM analysis was performed to the unknown and the reference problems. Here, the unknown problem is the problem to be analyzed, and the reference problem is the one whose exact solution is available. The unknown and the reference problems must be chosen so that they should have the identical singular stress field with different ISSF. Then, the FEM stress ratio of the unknown problem and the reference problem is focused since the FEM stress ratio may cancel the error included in FEM stress. In other words, by taking the FEM stress ratio, included FEM error can be canceled and the mesh dependency disappears since they have identical singular stress field but different ISSF [23–28]. The ISSF of an unknown problem can be obtained by multiplying the ratio of FEM stress and the ISSF of a reference problem chosen as the exact solution previously obtained. This analysis method is based on the fact the FEM stress distributions as well as the real singular stress fields are identical and proportional for the unknown and the reference problems [23–28]. Previously, Nisitani et al proposed the similar method to analyze crack stress intensity factors focusing on the FEM stress ratio at the crack tip named "the crack tip stress method" [54]. In this analysis, however, as can be shown later in Table C1, the focused FEM stress focused does not have to be located at the interface end.

From the discussion above, the ISSF ratio (e.g., $F^A_{\sigma,\lambda^A}/F^{A^*}_{\sigma,\lambda^A}$) of the reference problem and the unknown problem can be obtained as the FEM stress ratio (e.g., $\sigma^A_{FEM}(r)/\sigma^{A^*}_{FEM}(r)$) as can be expressed in Equation (C1). Here, $\sigma^{A^*}_{FEM}(r)$ is the stress distribution at point A* in the reference problem obtained by FEM analysis, and $\sigma^{B^*}_{I,FEM}(r)$ and $\sigma^{B^*}_{II,FEM}(r)$ are the mode I and mode II stress distributions at point B* in the reference problem obtained by FEM analysis, respectively. Also, $\sigma^A_{FEM}(r)$ is the stress distribution at point A in the unknown problem obtained by FEM analysis, and $\sigma^{B_i}_{I,FEM}(r)$ and $\sigma^{B_i}_{II,FEM}(r)$ are the mode I and mode II stress distributions at point B in the unknown problem obtained by FEM analysis, respectively.

$$\frac{F^A_{\sigma,\lambda^A}}{F^{A^*}_{\sigma,\lambda^A}} = \frac{\sigma^A_{FEM}(r)}{\sigma^{A^*}_{FEM}(r)},$$

$$\frac{F^{B_i}_{I,\lambda^B_1}}{F^{B^*}_{I,\lambda^B_1}} = \frac{\sigma^{B_i}_{I,FEM}(r)}{\sigma^{B^*}_{I,FEM}(r)},$$

$$\frac{F^{B_i}_{II,\lambda^B_2}}{F^{B^*}_{II,\lambda^B_2}} = \frac{\sigma^{B_i}_{II,FEM}(r)}{\sigma^{B^*}_{II,FEM}(r)} \tag{C1}$$

Table C1 shows the FEM stress distribution at Points A and B in the unknown problem obtained in Fig. A1 when the smallest mesh size $e_{min} = h/\left(3^4 \times 50\right)$ mm and $e_{min} = h/(3^5 \times 50)$ mm and the number of steps $N_S = 4$. Table C1(a) shows the FEM stress distribution $\sigma^A_{FEM}(r)$ around Point A in Fig. B1. Table C1(b) shows the FEM stress distribution of mode I $\sigma^{B_1}_{I,FEM}(r)$, and Table C1(c) shows the FEM stress distribution of mode II $\sigma^{B_1}_{II,FEM}(r)$. Those Tables also show the FEM stress ratios $\sigma^A_{FEM}(r)/\sigma^{A^*}_{FEM}(r), \sigma^{B_1}_{I,FEM}(r)/\sigma^{B^*}_{I,FEM}(r), \sigma^{B_1}_{II,FEM}(r)/\sigma^{B^*}_{II,FEM}(r)$.

From Table C1, it can be seen that the FEM stress distributions $\sigma^A_{FEM}(r), \sigma^{B_1}_{I,FEM}(r), \sigma^{B_1}_{II,FEM}(r)$ in Fig. B1 vary greatly depending on the mesh size. On the other hand, the FEM stress ratio distributions of Fig. B1 and of Fig.B2 $\sigma^A_{FEM}(r)/\sigma^{A^*}_{FEM}(r), \sigma^{B_1}_{I,FEM}(r)/\sigma^{B^*}_{I,FEM}(r), \sigma^{B_1}_{II,FEM}(r)/\sigma^{B^*}_{II,FEM}(r)$ are mesh-independent to the three significant digit. In other words, Table C1 clarifies that the ISSF of the unknown problem can be determined exactly by focusing on the FEM stress ratio distribution.

Table C1

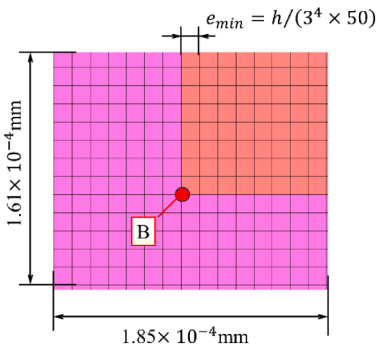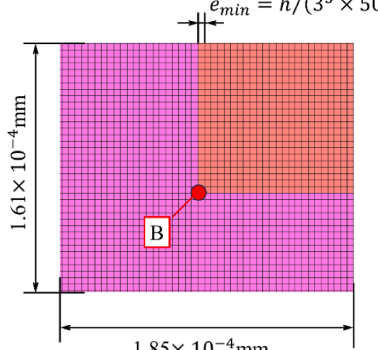Mesh independency of the present analysis method (h = adhesive thickness 0.05 mm).

(a) Ns = 4, Point A					
Smallest mesh size $e_{min} = h/(3^4 \times 50)mm$			Smallest mesh size $e_{min} = h/(3^5 \times 50)mm$		

r/e_{min}	$\sigma^A_{FEM}(r)$ [MPa]	$\dfrac{\sigma^A_{FEM}(r)}{\sigma^{A*}_{FEM}(r)}$	r/e_{min}	$\sigma^A_{FEM}(r)$ [MPa]	$\dfrac{\sigma^A_{FEM}(r)}{\sigma^{A*}_{FEM}(r)}$
0.0	6.166	0.988	0.0	8.538	0.988
0.5	3.022	0.988	0.5	4.189	0.988
1.0	2.191	0.988	1.0	3.044	0.988
1.5	2.100	0.988	1.5	2.920	0.988
2.0	2.024	0.988	2.0	2.817	0.988

(b) Ns = 4, Point B$_1$, Symmetrical type					
Smallest mesh size $e_{min} = h/(3^4 \times 50)mm$			Smallest mesh size $e_{min} = h/(3^5 \times 50)mm$		

r/e_{min}	$\sigma^A_{FEM}(r)$ [MPa]	$\dfrac{\sigma^A_{FEM}(r)}{\sigma^{A*}_{FEM}(r)}$	r/e_{min}	$\sigma^A_{FEM}(r)$ [MPa]	$\dfrac{\sigma^A_{FEM}(r)}{\sigma^{A*}_{FEM}(r)}$
0.0	32.60	3.400	0.0	52.42	3.398
0.5	6.450	3.401	0.5	10.33	3.401
1.0	-0.462	3.398	1.0	-0.809	3.398
1.5	-1.097	3.398	1.5	-1.842	3.398
2.0	0.709	3.400	2.0	1.056	3.398

Table C1 (*continued*)

(c) Ns = 4, Point B$_1$, Skew-Symmetrical type	
Smallest mesh size $e_{min} = h/(3^4 \times 50) mm$	Smallest mesh size $e_{min} = h/(3^5 \times 50) mm$

r/e_{min}	$\sigma^A_{FEM}(r)$ [MPa]	$\dfrac{\sigma^A_{FEM}(r)}{\sigma^{A*}_{FEM}(r)}$	r/e_{min}	$\sigma^A_{FEM}(r)$ [MPa]	$\dfrac{\sigma^A_{FEM}(r)}{\sigma^{A*}_{FEM}(r)}$
0.0	1.856	1.306	0.0	2.042	1.306
0.5	-0.004	1.308	0.5	-0.004	1.305
1.0	-0.048	1.306	1.0	-0.053	1.306
1.5	0.029	1.306	1.5	0.032	1.306
2.0	0.050	1.305	2.0	0.055	1.306

References

[1] X. Liu, G. Zheng, Q. Luo, Q. Li, G. Sun, Fatigue behavior of carbon fiber reinforced plastic and aluminum single-lap adhesive joints after the transverse pre-impact, Int. J. Fatigue 144 (2021) 105973.

[2] K. Kawajiri, M. Kobayashi, K. Sakamoto, Lightweight materials equal lightweight greenhouse gas emissions?: a historical analysis of greenhouse gases of vehicle material substitution, J. Clean. Prod. 253 (2019) 119805.

[3] A. Pramanik, A.K. Basak, Y. Dong, P.K. Sarker, M.S. Uddin, G. Littlefair, A.R. Dixit, S. Chattopadhyaya, Joining of carbon fiber reinforced polymer (CFRP) composites and aluminum alloys – A review, Compos. A Appl. Sci. Manuf. 101 (2017) 1–29.

[4] J.M. Arenas, C. Alía, J.J. Narbón, R. Ocaña, C. González, Considerations for the industrial application of structural adhesive joints in the aluminum–composite material bonding, Compos. B Eng. 44 (1) (2013) 417–423.

[5] S. Budhe, M.D. Banea, S. de Barros, L.F.M. da Silva, An updated review of adhesively 31 bonded joints in composite materials, Int. J. Adhes. Adhes. 72 (2017) 30–34.

[6] K. Naito, M. Onta, Y. Kogo, The effect of adhesive thickness on tensile and shear strength of polyimide adhesive'', Int. J. Adhes. Adhes. 36 (2012) 77–85.

[7] Z.X. Liu, Y.A. Huang, Z.P. Yin, S. Bennati, P.S. Valvo, A general solution for the two-dimensional stress analysis of balanced and unbalanced adhesively bonded joints, Int. J. Adhesion Adhesives 54 (2014) 112–123.

[8] M.A. Uddin, M.Y. Ali, H.P. Chan, Achieving optimum adhesion of conductive adhesive bonded flip-chip on flex packages, Rev. Adv. Mater. Sci. 21 (2) (2009) 165–172.

[9] Z. Huang, P. Kumar, I. Dutta, J.H.L. Pang, R. Sidhu, A general method ology for calculating mixed mode stress intensity factors and fracture toughness of solder joints with interfacial cracks, Eng. Fract. Mech. 131 (2014) 9–25.

[10] C. Morton, C.M. Spargo, V. Pickert, Electrified hydraulic power steering system in hybrid electric heavy trucks, IET Electr. Syst. Transp. 4 (3) (2014) 70–77.

[11] M. Yasuda, Mounting material systems for electronic devices, Hitachi Chem. Techn. Rep. 40 (2003) 1–7, in Japanese.

[12] M. Nakamura, Technological trends of epoxy molding compounds for advanced semiconductor packages, Panasonic Electron Eng. Techn. Jo. 56 (4) (2008) 9–16, in Japanese.

[13] N.A. Noda, G. Hotta, Y. Sano, Y. Takase, Mechanics and stress concentration for bonded dissimilar materials, Corona Publishing Co., Ltd, 2017 in Japanese.

[14] Y. Suzuki, Adhesion Engineering -Bonding and Joining of Dissimilar Materials, Improvement of Strength, Reliability and Durability, And Life Prediction Methods, Maruzen Publishing, 2018 (in Japanese).

[15] T. Shibutani, Evaluation of crack initiation at interfacial edge on the basis of fracture mechanics concept and application to electronics device, Jpn Inst. Electron. Packaging 7 (7) (2004) 639–644, in Japanese.

[16] M. Shiratori, Problems of joints in packaging of electronics devices, Trans. Jpn Soc. Mech. Eng. Ser. A 60 (577) (1994) 1905–1912.

[17] T. Hattori, S. Sakata, T. Hatsuta, H. Murakami, A stress singularity parameters approach for evaluating adhesive strength, Trans. Jpn Soc. Mech. Eng. 54 (499) (1988) 597–603 (in Japanese).

[18] C. Luangarpa, H. Koguchi, Singular stresses at a vertex and along a singular line in three-dimensional piezoelectric bonded joints, J. Appl. Comput. Mech. 6 (2020) 1364–1370. Special Issue.

[19] C. Luangarpa, H. Koguchi, Evaluation of intensities of singularity at three-dimensional piezoelectric bonded joints using a conservative integral, Eur. J. Mech. A/Solids 72 (2018) 198–208.

[20] W.K. Kim, T. Ikeda, N. Miyazaki, Analysis of delamination in a flip chip using anisotropic conductive adhesive film during moisture/reflow sensitivity test, Jpn Inst. Electron. Packaging 8 (3) (2005) 215–224, in Japanese.

[21] H. Hozoji, F. Kato, S. Tanaka, J. Shinkai, H. Sato, Power electronics packaging materials for high heat reliability, Jpn Inst. Electron. Packaging 24 (3) (2021) 233–240 (in Japanese).

[22] Y. Terao, T. Ouchi, S. Thinda, Rough electroplating Nickel technology for enhancement of adhesion between metals and plastic resin surface, Proceedings of MES2020, 1A4-3, 2020. (in Japanese).

[23] N.A. Noda, T. Miyazaki, R. Li, T. Uchikoba, Y. Sano, Y. Takase, Debonding strength evaluation in terms of the intensity of singular stress at the interface corner with and without fictitious crack, Int. J. Adhes. Adhes. 61 (2015) 46–64.

[24] N.A. Noda, F. Ren, R. Takaki, Z. Wang, K. Oda, T. Miyazaki, Y. Sano, Intensity of singular stress field over the entire bond line thickness range useful for evaluating the adhesive strength for plate and cylinder butt joints, Int. J. Adhes. Adhes. 85 (2018) 234–250.

[25] R. Takaki, N.A. Noda, Y. Suzuki, Y. Sano, K. Hirata, F. Ito, Cohesive failure verification and fracture origin identification when the adhesive strength is expressed as a constant ISSF, Int. J. Adhes. Adhes. 116 (2022) 103148.

[26] N.A. Noda, R. Li, T. Miyazaki, R. Takaki, Y. Sano, Convenient adhesive strength evaluation method in terms of the intensity of singular stress field, Int. J. Comput. Method 16 (1) (2019) 1850085.

[27] R. Li, N.A. Noda, R. Takaki, Y. Sano, Y. Takase, T. Miyazaki, Most suitable evaluation method for adhesive strength to minimize bend effect in lap joints in terms of the intensity of singular stress field, Int. J. Adhes. Adhes. 86 (2018) 45–58.

[28] N.A. Noda, R. Takaki, Y. Sano, B. Wang, ISSF method to evaluate adhesive strength when two distinct singular stress fields appear along the interface, Int. J. Fract. 241 (2023) 95–114.

[29] H. Bendemra, P. Compston, P.J. Crothers, Optimization study of tapered scarf and stepped-lap joints in composite repair patches, Compos. Struct. 130 (2015) 1–8.

[30] K.B. Katnam, L.F.M. Da Silva, T.M. Young, Bonded repair of composite aircraft structures: A review of scientific challenges and opportunities, Prog. Aerosp. Sci. 61 (2013) 26–42.

[31] K. Mori, H. Isono, T. Sugibayashi, Fracture behavior and strength of stepped-lap bonded joint with adhesive resin under tensile loading, Trans. Jpn Soc. Mech. Eng. Ser. A 60 (569) (1994) 71–79, in Japanese.

[32] K. Mori, T. Sugibayashi, Effect of number of steps on stress distribution and final fracture strength of stepped-lap bonded joint, Trans. Jpn Soc. Mech. Eng. Ser. A 55 (519) (1989) 2211–2219, in Japanese.

[33] F. Erdogan, M. Ratwani, Stress distribution in bonded joints, J. Compos. Mater. 378 (1971) 5–7.

[34] J.B. Cushman, S.F. McCleskey, S.H. Ward. Test and analysis of Celion 3000/PMR-15, Graphite/ Polyimide bonded composite joints: Data report, NASA CR-3602, 1983.

[35] L.J. Hart-Smith, Analysis and design of advanced composite bonded joints," NASA CR - 2218, 1974.

[36] N.A. Noda, B. Wang, S. Wang, R. Takaki, Y. Sano, Analysis of intensity of singular stress field at the stepped-lap joint, Jpn Inst. Electron. Packaging 24 (6) (2021) 595–605 (in Japanese).

[37] J. Zhou, Z.M. Huang, W. Xu, Prediction of laminate delamination from strength failure of interlaminar matrix-layer, J. Reinf. Plast. Compos. 42 (3–4) (2023) 177–187.

[38] S. Akpinar, The strength of the adhesively bonded step-lap joints for different step numbers, Compos. B 67 (2014) 170–178.

[39] D.B. Bogy, Edge-bonded dissimilar orthogonal elastic wedges under normal and shear loading, Trans. ASME, J. Appl. Mech. 35 (1968) 460–466.

[40] D.B. Bogy, Two edge-bonded elastic wedges of different materials and wedge angles under surface tractions, Trans. ASME, J. Appl. Mech. 38 (1971) 377–386.

[41] D.H. Chen, H. Nisitani, Singular stress field near the corner of jointed dissimilar materials, Trans. ASME, J. Appl. Mech. 60 (3) (1993) 607–613.

[42] J.H. Park, J.H. Choi, J.H. Kweon, Evaluating the strengths of thick aluminum-to-aluminum joints with different adhesive lengths and thicknesses, Compos. Struct. 92 (2010) 2226–2235.

[43] H. Nisitani, The two-dimensional stress problem solved using an electric digital computer, J. Soc. Mech. Eng. 70 (580) (1967) 627–635, in Japanese.

[44] H. Nisitani, The two-dimensional stress problem solved using an electric digital computer, Bull. JSME 11 (43) (1968) 14–23.

[45] D.H. Chen, H. Nisitani, Analysis of intensity of singular stress field at fiber end (1st Report, Method of analysis), Trans. Jpn Soc. Mech. Eng. Ser. A 58 (554) (1992) 1834–1838, in Japanese.

[46] D.H. Chen, H. Nisitani, Analysis of intensity of singular stress field at fiber end (2nd Report, Results of calculation), Trans. Jpn Soc. Mech. Eng. Ser. A 58 (555) (1992) 2153–2158, in Japanese.

[47] N.A. Noda, Q. Wang, Y. Uemura, Y. Kawashima, Singular integral equation method in the analysis of interaction between rectangular inclusions, Jpn Soc. Mech. Eng. Int. J. Ser. A 41 (3) (1998) 303–308.

[48] N.A. Noda, Y. Takase, M. Chen, Generalized stress intensity factors in the interaction between two fibers in matrix, Int. J. Fract. 103 (2000) 19–39.

[49] N.A. Noda, Y. Takase, T. Kamashima, Generalized stress intensity factors in the interaction within a rectangular array of rectangular inclusions, Arch. Appl. Mech. 73 (2003) 311–322.

[50] N.A. Noda, T. Genkai, Q. Wang, Intensity of singular stress fields at the end of a cylindrical inclusion, J. Appl. Mech. 70 (4) (2003) 487–495.

[51] N.A. Noda, Y. Takase, Intensity of singular stress at the fiber end in a hexagonal array of fibers, Int. J. Solids Struct. 42 (2005) 4890–4908.

[52] N.A. Noda, D. Chen, R. Takaki, A. Inoue, G. Zhang, Y. Sano, Intensity of singular stress fields of an embedded fiber under pull-out force, J. Soc. Mater. Sci., Jpn. 67 (12) (2018) 1073–1079, in Japanese.

[53] N.A. Noda, D. Chen, G. Zhang, Y. Sano, Single-fiber-pull-out analysis comparing the intensities of singular stress fields (ISSFs) at fiber end/entry points, Int. J. Mech. Sci. 165 (2020) 105196.

[54] H. Nisitani, T. Teranishi, KI of a circumferential crack emanating from an ellipsoidal cavity obtained by the crack tip stress method in FEM, Eng. Fract. Mech. 71 (4–6) (2004) 579–585.